

Marc O. Delchini^a, Jean C. Ragusa^{*,a}, Ray A. Berry^b

^a*Department of Nuclear Engineering, Texas A&M University, College Station, TX 77843, USA*

^b*Idaho National Laboratory, Idaho Falls, ID 83415, USA*

Abstract

aaa

Key words: aaa, bbb, ccc

1. Introduction

Over the past years an increasing interest raised for computational methods that can solve both compressible and incompressible flows. In engineering applications, there is often the need to solve for complex flows where a near incompressible regime or low Mach flow coexists with a supersonic flow domain. For example, such flow are encountered in aerodynamic in the study of airships. In the nuclear industry, flows are nearly the incompressible regime but compressible effects cannot be neglected because of the heat source and thus needs to be accurately resolved.

Because of the hyperbolic nature of the flow equations, numerical methods are required in order to accurately resolve shocks that can form during transonic and supersonic flows. Numerous numerical methods are available in the literature: flux-limiter, pressure-based viscosity method, Lapidus method, the entropy-viscosity method among others. These numerical methods are usually tested and developed using simple equation of states and for transonic and supersonic flows where the disparity between the acoustic waves and the fluid speed is not large since the Mach number is of order one.

2. The Entropy Viscosity Method

2.1. Background

In this section, the entropy-based viscosity method [1, 2, 3] is recalled for the multi-D Euler equations (with constant area A) [4]. As mentioned in Section 1 the entropy-based viscosity method consists of adding dissipative terms, with

*Corresponding author

Email addresses: `delchmo@tamu.edu` (Marc O. Delchini), `jean.ragusa@tamu.edu` (Jean C. Ragusa), `ray.berry@inl.gov` (Ray A. Berry)

23 a viscosity coefficient modulated by the entropy production which allows high-
 24 order accuracy when the solution is smooth. Thus, two questions arise: (i)
 25 how are the viscosity dissipative terms derived and (ii) how to numerically
 26 compute the entropy production. Answers to the first question can be found
 27 in [5] by Guermond et al., that details the proof leading to the derivation of
 28 the artificial dissipative terms (Eq. (1)) consistent with the entropy minimum
 29 principle theorem. The viscous regularization obtained is valid for any equation
 30 of state as long as the opposite of the physical entropy function is convex.

$$\begin{cases} \partial_t(\rho) + \vec{\nabla} \cdot (\rho \vec{u}) = \vec{\nabla} \cdot (\kappa \vec{\nabla} \rho) \\ \partial_t(\rho \vec{u}) + \vec{\nabla} \cdot (\rho \vec{u} \otimes \vec{u} + P \mathbf{I}) = \vec{\nabla} \cdot (\mu \rho \vec{\nabla}^s \vec{u} + \kappa \vec{u} \otimes \vec{\nabla} \rho) \\ \partial_t(\rho E) + \vec{\nabla} \cdot [\vec{u}(\rho E + P)] = \vec{\nabla} \cdot (\kappa \vec{\nabla}(\rho e) + \frac{1}{2} \|\vec{u}\|^2 \kappa \vec{\nabla} \rho + \rho \mu \vec{u} \vec{\nabla} \vec{u}) \\ P = P(\rho, e) \end{cases} \quad (1)$$

31 where κ and μ are local positive viscosity coefficients.
 32 The existence of a specific entropy s , function of the density ρ and the internal
 33 energy e is assumed. Convexity of $-s$ with respect to e and $1/\rho$ is required,
 34 along with the following equality verified by the partial derivatives of s : $P \partial_e s +$
 35 $\rho^2 \partial_\rho s = 0$.
 36 One crucial step remains a definition for the local viscosity coefficients μ and κ .
 37 In the current version of the method, κ and μ are set equal, so that the above
 38 viscous regularization (Eq. (1)) is equivalent to the parabolic regularization [6].
 39 The current definition includes a first-order viscosity coefficient referred to with
 40 the subscript *max*, and a high-order viscosity coefficient referred to with the
 41 subscript *e*. The first-order viscosity coefficients μ_{max} and κ_{max} are proportional
 42 to the local largest eigenvalue $\|\vec{u}\| + c$ and equivalent to an upwind-scheme, when
 43 used, which is known to be over-dissipative and monotone [7]:

$$\mu_{max}(\vec{r}, t) = \kappa_{max}(\vec{r}, t) = \frac{h}{2} (\|\vec{u}\| + c), \quad (2)$$

44 where h is the spatial grid size.
 45 The second-order viscosity coefficients κ_e and μ_e are set proportional to the
 46 entropy production that is evaluated by computing the local entropy residual
 47 D_e . It also includes the interfacial jump of the entropy flux J that will allow to
 48 detect any discontinuities other than shocks:

$$\mu_e(\vec{r}, t) = \kappa_e(\vec{r}, t) = h^2 \frac{\max(|D_e(\vec{r}, t)|, J)}{\|s - \bar{s}\|_\infty} \quad \text{with } D_e(\vec{r}, t) = \partial_t s + \vec{u} \cdot \vec{\nabla} s \quad (3)$$

49 where $\|\cdot\|_\infty$ and $\bar{\cdot}$ denote the infinite norm operator and the average operator
 50 over the entire computational domain, respectively. The definition of the jump
 51 J is discretization-dependent and examples of definition can be found in [4]
 52 for DGFEM. The denominator $\|s - \bar{s}\|_\infty$ is used for dimensionality purposes
 53 and should not be of the same order as h , on penalty of loosing the high-
 54 order accuracy. Currently, there are no theoretical justification for choosing the

denominator.

The definition of the viscosity coefficients μ and κ is function of the first- and second-order viscosity coefficients as follows:

$$\mu(\vec{r}, t) = \min(\mu_e(\vec{r}, t), \mu_{max}(\vec{r}, t)) \text{ and } \kappa(\vec{r}, t) = \min(\kappa_e(\vec{r}, t), \kappa_{max}(\vec{r}, t)). \quad (4)$$

This definition allows the following properties. In shock regions, the second-order viscosity coefficient experiences a peak because of entropy production, and thus, saturates to the first-order viscosity that is known to be over-dissipative and will smooth out oscillations. Anywhere else, the entropy production being small, the viscosity coefficients μ and κ are of order h^2 .

Using the above definition of the entropy-based viscosity method, high-order accuracy was demonstrated and excellent results were obtained with 1-D Sod shock tubes and various 2-D tests [1, 2, 4].

2.2. Issues in the Low-Mach Regime

In the Low-Mach Regime, the flow is known to be isentropic resulting in very little entropy production. Since the entropy viscosity method is directly based on the evaluation of the local entropy production, it will be interested to study how the entropy viscosity coefficients μ and κ scale in the low Mach regime. Mathematically, it means that the entropy residual D_e will be very small, so will be the denominator $\|s - \bar{s}\|_\infty$, thus making the ratio, used in the definition of the viscosity coefficients Eq. (3), undetermined. Therefore, the current definition of the viscosity coefficients seems unadapted to subsonic flow and could lead to ill-scaled dissipative terms. A solution would be to recast the entropy residual as a function of other variables in order to have more freedom in the choice of the normalization parameter. The idea is to still define the viscosity coefficient proportional to the entropy residual that is a good indicator of the flow type (subsonic or supersonic).

2.3. The dissipative-terms for the multi-D Euler equations with variable area

One of the focus of this paper is to investigate the application of the entropy viscosity method to the multi-D Euler equations with variable area: first, the dissipative terms are derived following (REF), and, the viscosity coefficients are defined. The full derivation can be found in APPENDIX and only the main steps are given here. The objective here is to assess whether or not the entropy viscosity method will accurately resolve a flow in a 1-D convergent-divergent nozzle (REFS with mine). In Section 5, 1-D results for liquid water in a nozzle are shown. This test is interesting for two reasons: (i) the flow under consideration is subsonic which is the focus of this paper, and, (ii) the flow reaches a steady-state and an exact-solution can be derived for this particular case (REF). Thus, a convergence study will be performed in order to show second-order accuracy.

The multi-D Euler equations degenerate to the multi-D Euler equations given in Eq. (1) when assuming constant area. The main difference lies in the momentum equation that contains a non-conservative term in the right-hand side. For the

96 purpose of this paper, the variable area is denoted by $A(\vec{r})$ and is only spatial
 97 dependent. The multi-D Euler equations with variable area are recalled (REF):

$$\begin{cases} \partial_t (\rho A) + \vec{\nabla} \cdot (\rho \vec{u} A) = 0 \\ \partial_t (\rho \vec{u} A) + \vec{\nabla} \cdot [A (\rho \vec{u} \otimes \vec{u} + P \mathbf{I})] = P \vec{\nabla} A \\ \partial_t (\rho E) + \vec{\nabla} \cdot [\vec{u} (\rho E + P)] = 0 \end{cases} \quad (5)$$

98 This system (Eq. (5)) admits the following entropy equation with the same
 99 entropy function as defined previously in Section 2.1:

$$\rho A \left(\partial_t s + \vec{u} \cdot \vec{\nabla} s \right) = 0$$

100 Once again, by adding dissipative terms in each equation of Eq. (5), the entropy
 101 equation is modified and by invoking the entropy minimum principle, adequate
 102 definition of the dissipative terms are derived as shown in Eq. (6):

$$\begin{cases} \partial_t (\rho A) + \vec{\nabla} \cdot (\rho \vec{u} A) = \vec{\nabla} \cdot (A \kappa \vec{\nabla} \rho) \\ \partial_t (\rho \vec{u} A) + \vec{\nabla} \cdot [A (\rho \vec{u} \otimes \vec{u} + P \mathbf{I})] = P \vec{\nabla} A + \vec{\nabla} \cdot \left[A \left(\mu \rho \vec{\nabla}^s \vec{u} + \kappa \vec{u} \otimes \vec{\nabla} \rho \right) \right] \\ \partial_t (\rho E) + \vec{\nabla} \cdot [\vec{u} (\rho E + P)] = \vec{\nabla} \cdot \left[A \left(\kappa \vec{\nabla} (\rho e) + \frac{1}{2} ||\vec{u}||^2 \kappa \vec{\nabla} \rho + \rho \mu \vec{u} \vec{\nabla} \vec{u} \right) \right] \end{cases} \quad (6)$$

103 The dissipative terms are very similar to the ones obtained for the multi-D Euler
 104 equations: each dissipative flux is multiplied by the variable area A in order to
 105 ensure conservation of the flux. When assuming a constant area, Eq. (1) is
 106 retrieved.

107 The definition of the viscosity coefficients is explained in Section 3.2. It is
 108 expected to have the same definition of the viscosity coefficients between the
 109 multi-D Euler equations with variable and constant area. This assumption is
 110 justified by the entropy residual for the variable area case: it can be obtained
 111 by simply multiplying the entropy residual of Eq. (3) by the area A . Thus, the
 112 variations of the entropy residual should be identical.

113 3. All-speed Reformulation of the Entropy Viscosity Method

114 In this section, it is shown how the entropy residual D_e can be recast as
 115 a function of the pressure, the density and the speed of sound. Then, an low
 116 Mach asymptotic study of the multi-D Euler equations is performed in order to
 117 derive the correct normalization parameter.

118 3.1. New Entropy Production Residual

119 The first step in defining a viscosity coefficient that behaves well in the low
 120 mach limit is to recast the entropy residual in terms of thermodynamic variables:

$$D_e(\vec{r}, t) = \partial_t s + \vec{u} \cdot \vec{\nabla} s = \frac{s_e}{P_e} \left(\underbrace{\frac{dP}{dt} - c^2 \frac{d\rho}{dt}}_{\tilde{D}_e(\vec{r}, t)} \right), \quad (7)$$

where $\frac{d}{dt}$ denotes the material or total derivative, and P_e is the partial derivative of pressure with respect to internal energy. The steps that lead to the new formulation of the entropy residual D_e can be found in APPENDIX.

The entropy residual D_e and \tilde{D}_e are proportional to each other and therefore will experience the same variation when taking the absolute value. Thus, locally evaluating \tilde{D}_e instead of D_e should allow us to measure the entropy production point wise. This new expression given in Eq. (7) has multiple advantages:

- an analytical expression of the entropy function is not longer needed: the entropy residual \tilde{D}_e is evaluated using the local values of the pressure, the density and the speed of sound. Deriving an entropy function for some complex equation of states can be difficult.
- with the proposed expression of the entropy residual function of pressure and density, additional normalizations suitable for low Mach flows of the entropy residual can be devised. Examples include the pressure itself, or combination of the density, the speed of sound and the norm of the velocity: ρc^2 , $\rho c||\vec{u}||$ and $\rho||\vec{u}||^2$.

The viscosity coefficients μ and κ are now defined proportional to the new entropy residual \tilde{D}_e on the model of Eq. (3) as follows:

$$\mu(\vec{r}, t) = \kappa(\vec{r}, t) = h^2 \frac{\max(\tilde{D}_e, J)}{n(P)} \quad (8)$$

where $n(P)$ is a normalization parameter to determine and all other variables were defined previously.

As mentioned earlier, the normalization parameter $n(P)$ must be of the same units as the pressure for the viscosity coefficients to have the unit of a dynamic viscosity (m^2/s). Multiples options are available to us (P , ρc^2 , $\rho c||\vec{u}||$ and $\rho||\vec{u}||^2$). The choice of the normalization parameter cannot be random if the definition of the viscosity coefficient is wanted to be well-scaled for a wide range of Mach numbers. For example, by choosing $n(P) = \rho||\vec{u}||^2$, the viscosity coefficient will become very large as the Mach number decreases which would be unnecessary since the equations will not develop any shock or discontinuity. Therefore, it is proposed to carry, in Section 3.2, a low-Mach asymptotic study of the multi-D Euler equations in order to determine the correct expression for the normalization parameter $n(P)$.

3.2. Low-Mach asymptotic study of the multi-D Euler equations

The asymptotic study requires the multi-D Euler equations to be non dimensionalized: the objective is to make the Mach number appears and thus, use a polynomial expansion of the variables as a function of the Mach number in order to derive the leading, first- and second-order equations. Before detailing the steps of the asymptotic method, let us have a closer look at the system of equations under consideration. The initial system of equations is composed of the multi-D Euler equations. For stability purpose, artificial dissipative terms

are added to each equation as explained in Section 2. The resulting system of equations is alike the multi-D Navier-Stokes equations in a sense that it contains second-order derivative terms. Thus, it would be interesting to look at the steps employed in the asymptotic study of the multi-D Navier-Stokes equations in order to understand how the dissipative terms are treated. Fortunately, this process is well-documented in the literature (REFS) for both multi-D Euler equations and Navier-Stokes equations. The work presented here is mainly inspired of (REF) that focuses on the asymptotic study in the low Mach regime of Navier-Stokes equations. During the derivation, the reader has to keep in mind that the objective of this section is to derive a normalization parameter for the definition of the viscosity coefficients so that the multi-D Euler equations degenerate to the incompressible system of equations, which implies that the dissipative terms are well-scaled. The full derivation that leads to the final result can be found in APPENDIX. In this section, only the main steps are recalled.

To express Eq. (1) in dimensionless variables, the following definitions are used

$$\begin{aligned}\rho &= \frac{\rho^*}{\rho_\infty}, P = \frac{P^*}{\rho_\infty c_\infty^2}, \mu = \frac{\mu^*}{\mu_\infty}, E = \frac{E^*}{c_\infty^2}, \mu = \frac{\mu^*}{\mu_\infty}, \\ \kappa &= \frac{\kappa^*}{\kappa_\infty}, x = \frac{x^*}{L_\infty}, t = \frac{t^*}{L_\infty/u_\infty}, u = \frac{u^*}{u_\infty}\end{aligned}\quad (9)$$

where the subscript ∞ and the upper script $*$ denote far field or stagnation quantities and the dimensionless variables, respectively. The reference quantities are chosen such that the non dimensional flow quantities are of order one for any low reference-Mach number

$$M_\infty = \frac{u_\infty^*}{c_\infty^*} \quad (10)$$

where c_∞^* is a reference value for the speed of sound.

Then, using the non dimensional quantities and the multi-D Euler equations from Eq. (1), the following non dimensional form is obtained:

$$\begin{cases} \partial_t \rho + \nabla \cdot (\rho \vec{u}) = \frac{1}{Re_\infty Pr_\infty} \nabla \cdot (\kappa \nabla \rho) \\ \partial_t (\rho \vec{u}) + \nabla \cdot (\rho \vec{u} \otimes \vec{u}) + \frac{1}{M_\infty^2} \nabla (P) = \frac{1}{Re_\infty} \nabla \cdot (\rho \mu \nabla \vec{u}) + \frac{1}{Re_\infty Pr_\infty} \nabla \cdot (\vec{u} \otimes \kappa \nabla \rho) \\ \partial_t (\rho E) + \nabla \cdot [\vec{u} (\rho E + P)] = \frac{1}{Re_\infty Pr_\infty} \nabla \cdot (\kappa \nabla (\rho e)) + \frac{\tilde{M}_\infty^2}{Re_\infty} \nabla \cdot (\vec{u} \rho \mu \nabla \vec{u}) \\ + \frac{M_\infty^2}{2 Re_\infty Pr_\infty} \nabla \cdot (\kappa u^2 \nabla \rho) \\ P = (\gamma - 1) (\rho E + M_\infty^2 \rho u^2) \end{cases}$$

where the *numerical* Reynolds (Re_∞) and Prandtl (Pr_∞) numbers are defined as follows:

$$Re_\infty = \frac{u_\infty L_\infty}{\mu_\infty} \text{ and } Pr_\infty = \frac{\mu_\infty}{\kappa_\infty}. \quad (11)$$

Since it is chosen to have the same definition for both μ and κ the numerical Prandtl number is unconditionally equal to one: $Pr_\infty = 1$.

187 Once the dimensionless equations are obtained, the next step consists of expand-
 188 ing each variable in term of the Mach number (example given in Eq. (12) for
 189 the pressure P) in order to derive the leading, first- and second-order equations.

$$P(\vec{r}, t) = P_0(\vec{r}, t) + P_1(\vec{r}, t)M_\infty + P_2(\vec{r}, t)M_\infty^2 + \dots \text{ with } M_\infty \rightarrow 0 \quad (12)$$

190 Before deriving the leading-order equation, a choice needs to be made on how
 191 the numerical Reynolds number scales. Multiple options are available to us and
 192 a few example are given: $Re_\infty = M_\infty$, or $Re_\infty = M_\infty^{-1}$ or $Re_\infty = 1$. Let us
 193 assume for academy purpose that the numerical Reynolds number scales as the
 194 inverse of the Mach number square: $Re_\infty = M_\infty^{-2}$. The best way to evaluate the
 195 impact of this choice on the equations, is to look at the momentum equation
 196 and try to derive the order M_∞^{-2} :

$$\vec{\nabla} P_0 = \vec{\nabla} \cdot (\rho_0 \mu_0 \vec{\nabla} \vec{u}_0 + \vec{u}_0 \otimes \vec{\nabla} \rho_0) \quad (13)$$

197 which is known to be (REF)

$$\vec{\nabla} P_0 = 0 \quad (14)$$

198 It is clear that Eq. (13) and Eq. (14) will not yield the same result. The same
 199 conclusion is drawn when deriving the order M_∞^{-1} of the momentum equation,
 200 making our initial assumption not suitable. From the above result, it is under-
 201 stood that the numerical Reynolds number has to scale as one so that it does
 202 not affect the orders M_∞^{-2} and M_∞^{-1} of the momentum equations: $Re_\infty = 1$.
 203 Thus, with such assumption, Eq. (11) implies:

At order M_∞^{-2} :

$$\vec{\nabla} P_0 = 0$$

At order M_∞^{-1} :

$$\vec{\nabla} P_1 = 0$$

At leading-order:

$$\begin{aligned} \partial_t \rho_0 + \vec{\nabla} \cdot (\rho_0 \vec{u}_0) &= \vec{\nabla} \cdot (\kappa_0 \vec{\nabla} \rho_0) \\ \partial_t (\rho_0 \vec{u}_0) + \vec{\nabla} \cdot (\rho_0 \vec{u}_0 \otimes \vec{u}_0) + \vec{\nabla} P_2 &= \vec{\nabla} \cdot (\rho_0 \mu_0 \vec{\nabla} \vec{u}_0 + \vec{u}_0 \otimes \vec{\nabla} \rho_0) \\ \partial_t (\rho_0 E_0) + \vec{\nabla} \cdot [\vec{u}_0 (\rho_0 E_0 + P_0)] &= \vec{\nabla} \cdot (\kappa_0 \vec{\nabla} (\rho_0 e_0)) \end{aligned}$$

204 Under this form, the dissipative terms are well-scaled and should not alter the
 205 physical solution in the asymptotic limit.

206 It is now determined that the numerical Reynolds number Re_∞ has to scale as
 207 one. Following Eq. (11), Re_∞ is a function of the μ_∞ , and thus n_P . It can be
 208 shown using Eq. (9) and the definitions of \tilde{D} given in Eq. (7) that:

$$\mu_\infty = \frac{\rho_\infty c_\infty^2 u_\infty L}{n_{P,\infty}} \quad (15)$$

209 where $n_{P,\infty}$ is the far-field quantity for the normalization parameter n_P . Sub-
 210 stituting Eq. (15) into Eq. (11) and remembering that the numerical Reynolds

number scales as one, it yields:

$$n_{P,\infty} = \rho_\infty c_\infty^2 \quad (16)$$

Eq. (16) tells us that in the asymptotic limit, the normalization parameter n_P scales as $\rho_\infty c_\infty^2$ which leaves us with two options: either $n_P = \rho c^2$ or $n_P = P$. The choice was made to use $n_P = \rho c^2$ in the asymptotic limit (it was found to behave well as shown in Section 5) which, we believe, is more representative of the flow type. This definition is only valid in the asymptotic limit and the purpose of this paper is to define a viscosity coefficient μ that is valid for a wide range of Mach numbers. Thus, it is proposed to define the high-order viscosity coefficient μ_e as follows:

$$\mu_e = h^2 \frac{\max(\tilde{D}_e, J)}{(1 - f(M))\rho c^2 + f(M)\rho \|\vec{u}\|^2} \quad (17)$$

where $f(M)$ is a function of the local Mach number M with the following properties:

$$\begin{cases} f(M) \rightarrow 0 \text{ as } M \rightarrow 0 \\ f(M) \rightarrow 1 \text{ as } M \geq 1 \end{cases} \quad (18)$$

The choice of the function $f(M)$ is not fixed and a few examples are available in the literature. (REF) proposed the simple definition $f(M) = \min(M, 1)$ which meets the conditions of Eq. (18). Another definition for $f(M)$ was proposed by (REF):

$$f(M) = \quad (19)$$

All of the numerical results presented in Section 5 were obtained by using $f(M) = \min(M, 1)$ which is simple to implement. A convergence test for a subsonic flow over a 2-D cylinder will show that this definition of $f(M)$ yields the correct behavior in the asymptotic limit. The definition of the high-order viscosity coefficient $\mu_e(\vec{r}, t)$ should behave well for complex flow where a near incompressible regime coexists with a supersonic flow domain since $f(M)$ is function of the local Mach number.

For clarity purpose, the full definition of the viscosity coefficient $\mu(\vec{r}, t)$ is recalled:

$$\begin{cases} \mu(\vec{r}, t) = \max(\mu_{max}(\vec{r}, t), \mu_e(\vec{r}, t)) \\ \text{where } \mu_{max}(\vec{r}, t) = \frac{h}{2}(\|\vec{u}\| + c) \\ \text{and } \mu_e(\vec{r}, t) = h^2 \frac{\max(\tilde{D}_e, J)}{(1 - f(M))\rho c^2 + f(M)\rho \|\vec{u}\|^2} \\ \mu(\vec{r}, t) = \kappa(\vec{r}, t) \end{cases} \quad (20)$$

These viscosity coefficients are valid for both the multi-D Euler equations with variable and constant area and are employed with the dissipative terms detailed in Eq. (11). The reader will notice that, through the derivation, none assumption was made on the type of equation of state besides the convexity condition on the entropy function s . The remaining of this paper (Section 5) will focus on demonstrating that the definition of the viscosity coefficient given in Eq. (20) is indeed well-scaled in the asymptotic limit and that shocks are still well resolved.

242 4. Solution Techniques Spatial and Temporal Discretizations

243 In order to detail the partial and temporal discretization used for this study,
 244 the system of equations presented in Section 1 is considered under the following
 245 form:

$$\partial_t U + \vec{\nabla} \cdot F(U) = S \quad (21)$$

246 where U is the vector solution, F is a conservative vector flux and S is a vec-
 247 tor source that can contain some relaxation source terms and non-conservative
 248 terms.

249 4.1. Spatial and Temporal Discretizations

250 The system of equation given in Eq. (21) is discretized using a continuous
 251 Galerkin finite element method and high-order temporal integrators provided
 252 by the MOOSE framework.

253 4.1.1. CFEM

254 In order to apply the continuous finite element method, Eq. (21) is multiplied
 255 by a smooth test function ϕ , integrated by part and each integral is split onto
 256 each finite element e of the discrete mesh Ω bounded by $\partial\Omega$, to obtain a weak
 257 solution:

$$\sum_e \int_e \partial_t U \phi - \sum_e \int_e F(U) \cdot \vec{\nabla} \phi + \int_{\partial\Omega} F(U) \vec{n} \phi - \sum_e \int_e S \phi = 0 \quad (22)$$

258 The integrals over the elements e are evaluated using quadrature-point rules.
 259 The Moose framework provides a wide range of test function and quadrature
 260 rules: trapezoidal and Gauss rules among others. Linear Lagrange polynomials
 261 will be used as test functions and should ensure second-order convergence for
 262 smooth functions. The order of convergence will be demonstrated.

263 4.1.2. Temporal integrator

264 The MOOSE framework offers both first- and second-order explicit and im-
 265 plicit temporal integrators. In all of the numerical examples presented in Sec-
 266 tion 5, the time-dependent term $\int_e \partial_t U \phi$ will be evaluated using the second-order
 267 temporal integrator BDF2. By considering three converged solutions, U^{n-1} , U^n
 268 and U^{n+1} at three different time t^{n-1} , t^n and t^{n+1} , respectively, it yields:

$$\int_e \partial_t U \phi = \omega_0 U^{n+1} + \omega_1 U^n + \omega_2 U^{n-1} \quad (23)$$

with $\omega_0 = \frac{3}{2}$, $\omega_1 = -2$ and $\omega_2 = \frac{1}{2}$

269 4.2. Boundary conditions

270 The boundary conditions will be treated by either using Dirichlet or Neu-
271 mann conditions. The multi-D Euler equations are wave-dominated systems
272 that require great care when dealing with boundary conditions. It is often rec-
273 ommended to use the characteristic equations to compute the correct flux at
274 the boundaries. Our implementation of the boundary conditions will follow the
275 method described in [8] that was developed for Ideal Gas and Stiffened Gas
276 equation of states. For each numerical solution presented in Section 5, the type
277 of boundary conditions used will be specified.

278 4.3. Solver

279 A Free-Jacobian-Newton-Krylov (FJNK) method is used to solve for the
280 solution at each time step.

281 5. Numerical Results

282 This section aims at validating our approach detailed in Section 3.2 that
283 focused on deriving a viscosity coefficient behaving well in the asymptotic limit.
284 It is proposed to run both 1- and 2-D simulations. The 1-D simulations consist
285 of liquid water and steam flowing in a convergent-divergent nozzle. This test is
286 interesting for multiple reasons: a steady-state is reached, it can be performed
287 for liquid and gas phases and an analytical solution of the steady-state solution
288 is available. Numerical results for the challenging Leblanc shock tube are also
289 shown (REF). Subsonic flows of a gas over a 2-D cylinder and a hump are
290 simulated and results are shown for various far-field Mach numbers. Numerical
291 results of a supersonic flow in a compression corner are provided to illustrate the
292 capabilities of the new definition in the supersonic case. Convergence studies
293 are performed when an analytical solution is available. For each simulation,
294 informations relative to the boundary conditions and the equation of state will
295 be provided. All of the numerical solution presented in this section are run
296 with the second-order temporal integrator *BDF2* and linear polynomials test
297 function and integrated with a Gauss second-order quadrature rule.

298 5.1. Liquid water in a 1-D divergent-convergent nozzle

299 The liquid water phase is simulated using the Stiffened gas equation of state
300 (REF). The following parameters are used:
301 The simulation consists of a 1 convergent-divergent nozzle with the following
302 equation, $A(x) = 1 + 0.5 \cos(2\pi x/L)$, where $L = 1m$ is the length of the nozzle.
303 At the inlet, a stagnation pressure boundary condition is used: the stagnation
304 pressure and temperature are set to $P_0 = 1MPa$ and $T_0 = 453K$, respectively.
305 At the outlet, only the static pressure is specified, $P_s = 0.5MPa$. Details about
306 the theory related to the inlet and outlet boundary conditions can be found in
307 (REFS). Initially, the temperature is uniform and set equal to the stagnation
308 temperature and the pressure linearly decreases from the stagnation pressure to

the static one. Finally, the liquid is assumed at rest. The Stiffened Gas equation of state is used to model liquid water with the parameters provided in Table 1.

Table 1: Stiffened Gas Equation of State parameters for liquid water.

γ	$C_v (J \cdot kg^{-1} \cdot K^{-1})$	$P_\infty (Pa)$	$q (J \cdot kg^{-1})$
2.35	1816	10^9	-1167.10^3

Plots of the pressure, velocity and density are given at steady-state and during the transient. The viscosity coefficients are also plotted but only at steady-state. Since a steady-state analytical solution is available to us (REF), a convergence study is performed in order to demonstrate the accuracy of the entropy viscosity method. For the liquid phase, the solution corresponds to a low-Mach regime case: the flow is isentropic and the final solution does not display any shock or discontinuity. This is a good test to assess the behavior of the new definition of the viscosity coefficient proposed in Eq. (20). Plots of the velocity, pressure, density and viscosity coefficients at steady-state are given in Fig. 1a, Fig. 1b, Fig. 1c and Fig. 1d, respectively. The exact solution is also plotted for comparison. The mesh used is uniform and has 50 cells. The final solution being smooth, a coarse mesh should be sufficient to capture the main features.

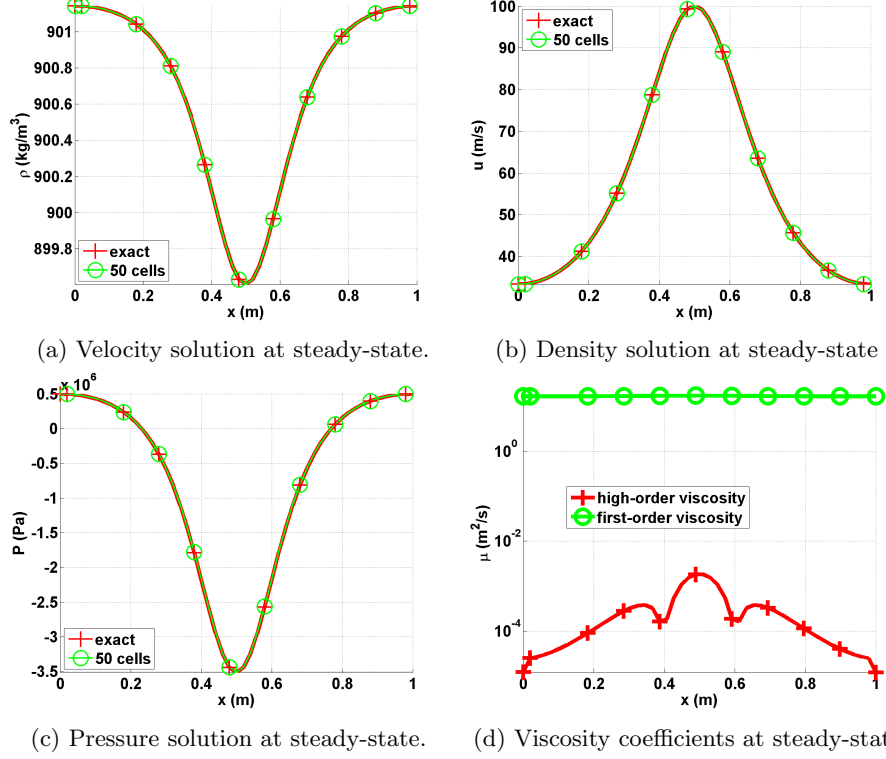


Figure 1: Steady-state solution for liquid phase in a 1-D convergent-divergent nozzle with an uniform mesh of 50 cells.

324 The numerical and exact solutions of the velocity, pressure and density given
 325 in Fig. 1 for a fairly coarse mesh (50 cells) perfectly overlap: it is noted that
 326 the numerical solution is symmetric with respect to the nozzle throat located
 327 in $x = 0.5m$. The second-order viscosity coefficient is very small compare to
 328 the first-order one as expected: (i) the numerical solution is smooth as shown
 329 in Fig. 1d and (ii) the flow is in a low Mach regime and thus isentropic . A
 330 convergence study was performed using the exact solution as a reference: the
 331 L2 norm of the error and the corresponding convergence rates are computed at
 332 steady-state on various uniform mesh from 4 to 256 cells. The results for linear
 333 polynomials \mathbb{Q}_1 is reported in Table 2.

Table 2: L2 norm of the error for the liquid phase in a 1-D convergent-divergent nozzle at steady-state.

cells	density	rate	pressure	rate	velocity	rate
4	$3.106397 \cdot 10^{-1}$	—	$5.254445 \cdot 10^5$	—	3.288543	—
8	$7.491623 \cdot 10^{-2}$	2.07	$1.636966 \cdot 10^5$	1.60	1.823880	0.90
16	$2.079858 \cdot 10^{-2}$	1.80	$4.627338 \cdot 10^4$	1.75	$4.990605 \cdot 10^{-1}$	1.83
32	$5.329627 \cdot 10^{-3}$	1.90	$1.180287 \cdot 10^4$	1.92	$1.261018 \cdot 10^{-1}$	1.93
64	$1.341583 \cdot 10^{-3}$	1.94	$2.967104 \cdot 10^3$	1.98	$3.160914 \cdot 10^{-2}$	1.99
128	$3.359766 \cdot 10^{-4}$	1.99	$7.428087 \cdot 10^2$	1.99	$7.907499 \cdot 10^{-3}$	1.99
256	$8.403859 \cdot 10^{-5}$	1.99	$1.857861 \cdot 10^2$	1.99	$1.977292 \cdot 10^{-3}$	1.99

334 It is observed that the convergence rate for the L2 norm of the error is 2: the
 335 entropy viscosity method conserves the high-order accuracy when the numerical
 336 solution is smooth, and the new definition of the entropy viscosity coefficient
 337 seems to behave as expected in the low Mach limit.

338 5.2. Steam in a 1-D divergent-convergent nozzle

339 The results of this section are obtained using the exact same 1-D geometry,
 340 initial condition and boundary conditions as in Section 5.1. The Stiffened gas
 341 equation of state is still used but with different parameters that are given in
 342 Table 3.

Table 3: Stiffened Gas Equation of State parameters for steam.

γ	$C_v (J \cdot kg^{-1} \cdot K^{-1})$	$P_\infty (Pa)$	$q (J \cdot kg^{-1})$
1.43	1040	0	$2030 \cdot 10^3$

343 The pressure difference applied between the inlet and outlet will make the
 344 steam accelerates through the nozzle and result in the formation of shock in the
 345 divergent part. The behavior is different from what is observed for the liquid
 346 water phase in Section 5.1 because of the liquid to gas density ratio that is of
 347 1000. The objective of this section is to show that using the new definition of
 348 the viscosity coefficient in Eq. (20), the shock can be correctly resolved without
 349 spurious oscillation. The steady-state numerical solution is shown in Fig. 2 and
 350 was run with a mesh of 1600 cells.

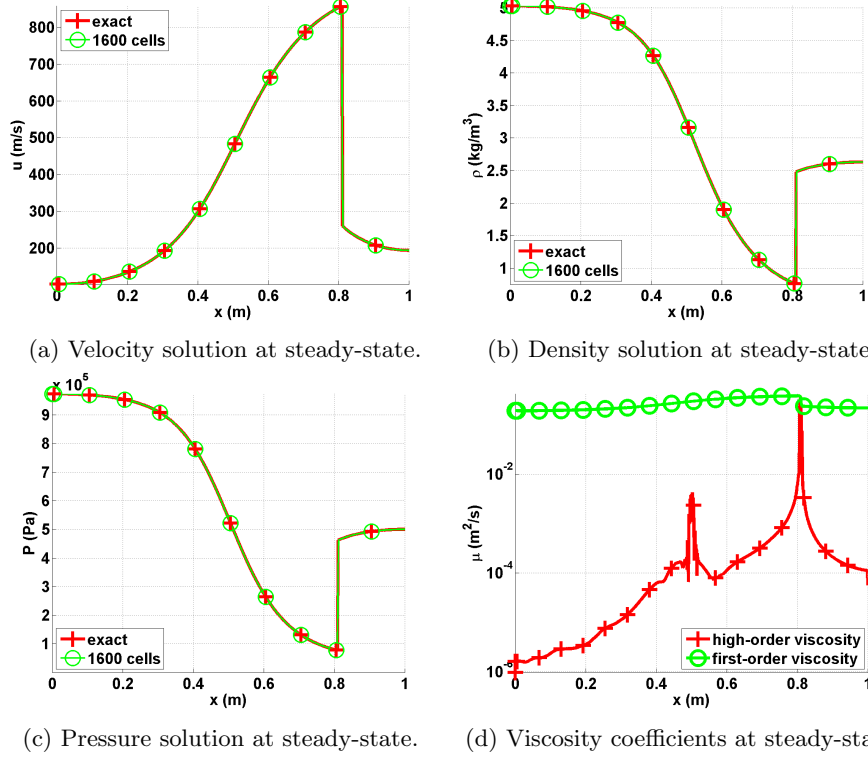


Figure 2: Steady-state solution for vapor phase in a 1-D convergent-divergent nozzle.

351 The steady-state solution of the density, velocity and pressure are given
 352 in Fig. 2a, Fig. 2b and Fig. 2c. The steady-solution displays a shock around
 353 $x = 0.8m$ and match the exact solution. In Fig. 2d, the first- and second-
 354 order viscosity coefficients are log plotted at steady-state: the second-order
 355 viscosity coefficient is peaked in the shock region around $x = 0.8m$ as expected,
 356 and saturate to the first-order viscosity coefficient. The profile also displays
 357 another peak at $x = 0.5m$ that corresponds to the position of the sonic point for a 1-
 358 D convergent-divergent nozzle: this particular point is known to develop small
 359 instabilities that are detected when computing the jumps of the pressure and
 360 density gradients. Anywhere else, the second-order viscosity coefficient is small.
 361 In order to prove convergence of the numerical solution to the exact solution, a
 362 convergence study was performed. Because of the presence of a shock, second-
 363 order accuracy cannot be achieved. However, the convergence rate is known
 364 and expected to be of $1/2$ when computing the L2 norm of the error. Results
 365 are provided in ...

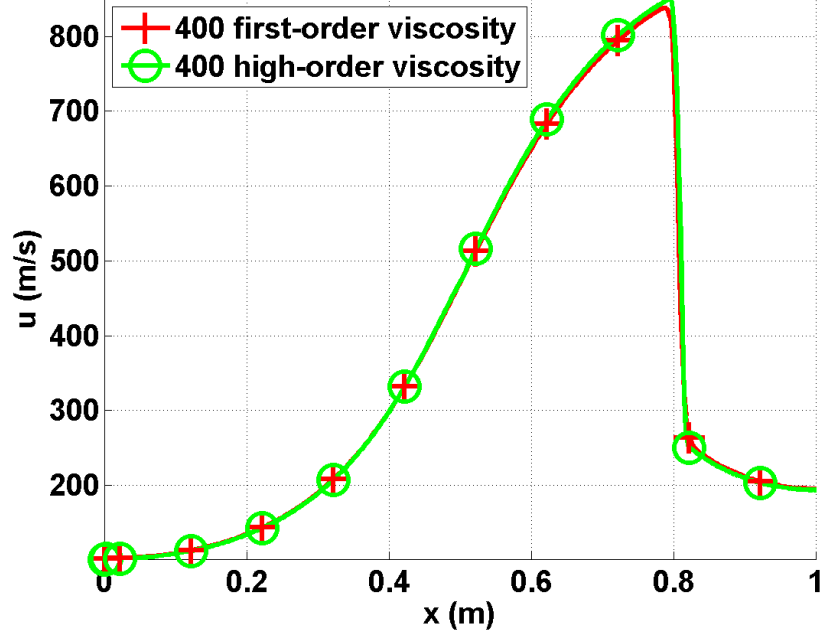


Figure 3: Velocity profile at steady-state with the first- and second-order viscosity for a mesh with 400 cells.

366 In Fig. 3, the steady-state velocity profile is plotted when using the first-
 367 and second-order viscosity coefficients: the main difference between the two
 368 numerical solution is in the resolution of the shock around $x = 0.8m$. The
 369 first-order viscosity coefficient is by definition more dissipative and will smooth
 370 out the solution. In the other hand, the high-order viscosity better resolves the
 371 shock and allow high-order accuracy away from the shock region. It is also noted
 372 that the numerical solution obtained with the first-order viscosity coefficient is
 373 satisfying: this is due to the nature of the solution that contains a standing
 374 shock, and thus, will force the shock to form.

375 5.3. Leblanc shock tube

376 The 1-D Leblanc shock tube is a Riemann problem and designed to test the
 377 robustness and the accuracy of the stabilization method. The initial conditions
 378 are given in Table 4. The ideal gas equation of state is used to compute the
 379 fluid pressure with the following heat capacity ratio $\gamma = 5/3$.

Table 4: Initial conditions for the 1-D Leblanc shock tube.

	ρ	u	e
left	1.	0.	0.1
right	10^{-3}	0.	10^{-7}

380 This test is computationally challenging because of the large left to right
381 pressure ratio. The computational domain consists of a 1-D pipe of length
382 $L = 9m$ with an interface located at $x = 2m$. At $t = 0.s$, the interface is
383 removed, allowing the fluid to move. The numerical solution is run until $t = 4.s$
384 and the density, velocity and pressure profiles are given in Fig. 4a, Fig. 4b
385 and Fig. 4c, respectively. The viscosity coefficients are also plotted in Fig. 4d.
386 These plots were obtained with a mesh of 6000 cells and a constant time step
387 $\Delta t = 10^{-3}s$.

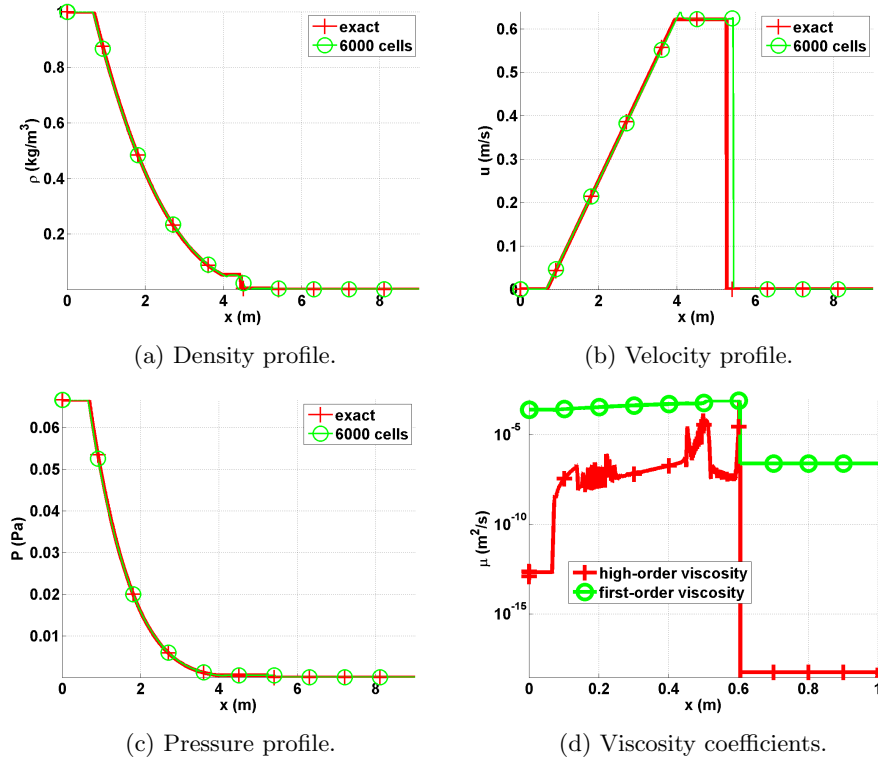


Figure 4: Numerical solution for the 1-D Leblanc shock tube at $t = 4.s$.

388 The pressure, density and velocity profiles given in Fig. 4 do not display any
389 oscillations. In Fig. 4c and Fig. 4b, the shock region is zoomed in for better
390 resolution: the shock is well resolved and no oscillation is observed. It is also

391 observed that the shock position is function of the mesh and converges to the
 392 exact position when refining the mesh. The contact wave is shown in Fig. 4b at
 393 $x = 4.5m$. The second-order viscosity coefficient profile is shown in Fig. 4d and
 394 behaves as expected: it saturates to the first-order viscosity in the shock region
 395 and thus prevent oscillations from forming. In the contact wave at $x = 4.5m$, a
 396 smaller peak is observed that is due to the presence of the jumps in the definition
 397 of the second-order viscosity coefficient (Eq. (20)).
 398 Once again, a convergence study is performed in order to prove convergence of
 399 the numerical solution to the exact solution. As for the vapor phase in the 1-D
 400 nozzle (Section 5.2), the expected convergence rate for the L2 and L1 norms
 401 of the error are $1/2$ and 1 , respectively. The exact solution was obtained by
 402 running a 1-D Riemann solver and used as a reference solution to compute the
 403 L2 and L1-norms given in Table 5.

Table 5: L2 norm of the error for the 1-D Leblanc test at $t = 4.s$.

cells	density	rate	pressure	rate	velocity	rate
500	$3.106397 \cdot 10^{-1}$	—	$5.254445 \cdot 10^5$	—	3.288543	—
1000	$7.491623 \cdot 10^{-2}$	0.64781	$1.636966 \cdot 10^5$	0.58793	1.823880	0.89392
2000	$2.079858 \cdot 10^{-2}$	0.70756	$4.627338 \cdot 10^4$	0.53448	$0.53448 \cdot 10^{-1}$	0.77533
3000	$5.329627 \cdot 10^{-3}$	0.64117	$1.180287 \cdot 10^4$	0.58506	$0.58506 \cdot 10^{-1}$	0.72276
4000	$1.341583 \cdot 10^{-3}$	0.58965	$2.967104 \cdot 10^3$	0.56103	$0.56103 \cdot 10^{-2}$	0.60112
5000	$3.359766 \cdot 10^{-4}$	0.54925	$7.428087 \cdot 10^2$	0.55095	$0.55095 \cdot 10^{-3}$	0.55351
6000	$8.403859 \cdot 10^{-5}$	0.31882	$1.857861 \cdot 10^2$	0.44813	$0.44813 \cdot 10^{-3}$	0.15305
7000	$8.403859 \cdot 10^{-5}$	0.51148	$1.857861 \cdot 10^2$	0.52587	$0.52587 \cdot 10^{-3}$	0.50216
8000	$8.403859 \cdot 10^{-5}$	0.50469	$1.857861 \cdot 10^2$	0.52459	$0.52459 \cdot 10^{-3}$	0.50189
9000	$8.403859 \cdot 10^{-5}$	0.51019	$1.857861 \cdot 10^2$	0.51622	$0.51622 \cdot 10^{-3}$	0.52773

404 The convergence rates are close to the expected values which prove conver-
 405 gence of the numerical solution to the exact solution.

406 5.4. Subsonic flow over a 2-D cylinder

407 The flow of a fluid over a 2-D cylinder is a typical benchmark case to test
 408 the behavior of a numerical method in the low Mach regime. For this test, an
 409 analytical solution is available in the incompressible limit or low Mach limit
 410 (REFS) and often referred to as potential flow. The numerical solution can be
 411 compared against the analytical solution in order to evaluate the effect of the
 412 numerical dissipation. The main features of the potential flow are the following:

- 413 • The solution is symmetric: the iso-mach number lines are used to asses
 414 the symmetry of the numerical solution.
- 415 • The velocity at the top of the cylinder is twice the incoming velocity set
 416 at the inlet.

- 417 • The pressure fluctuations are proportional to the inlet Mach number square,
 418 as follows:

$$\tilde{P} = \frac{\max(P) - \min(P)}{\max(P)} \propto M_{\infty}^2$$

419 where \tilde{P} and M_{∞} are the pressure fluctuations and the inlet Mach number,
 420 respectively.

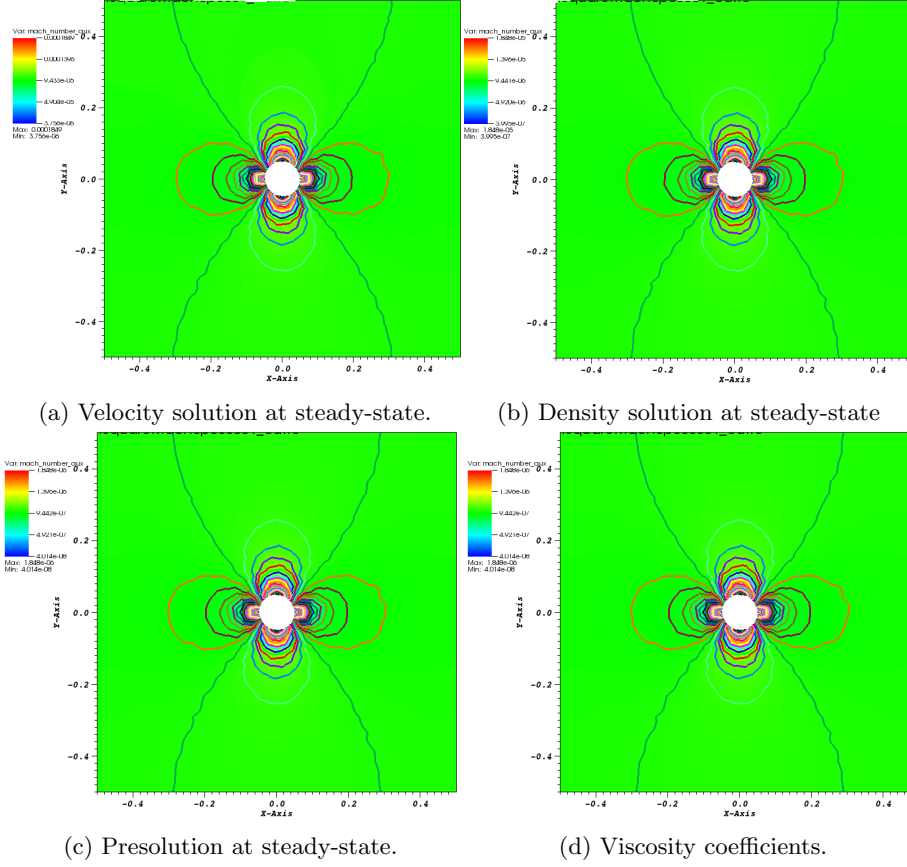


Figure 5: Steady-state solution for vapor phase in a 1-D convergent-divergent nozzle.

421 *5.5. Subsonic flow over a 2-D hump*

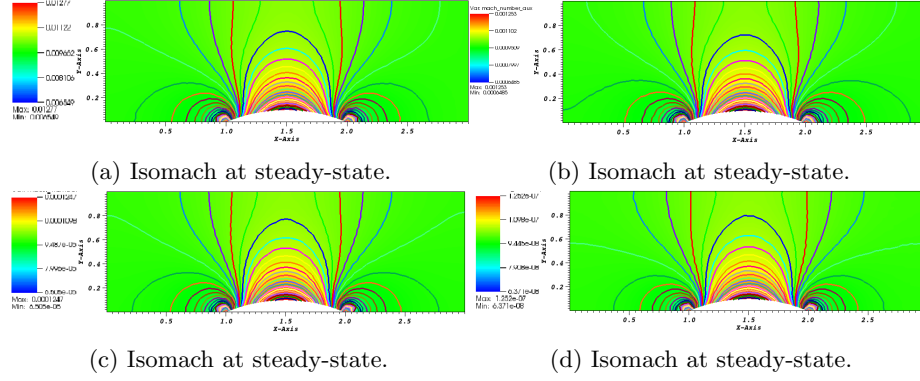


Figure 6: Steady-state solution for a flow in a 2-D compression corner.

422 *5.6. Supersonic flow in a compression corner*

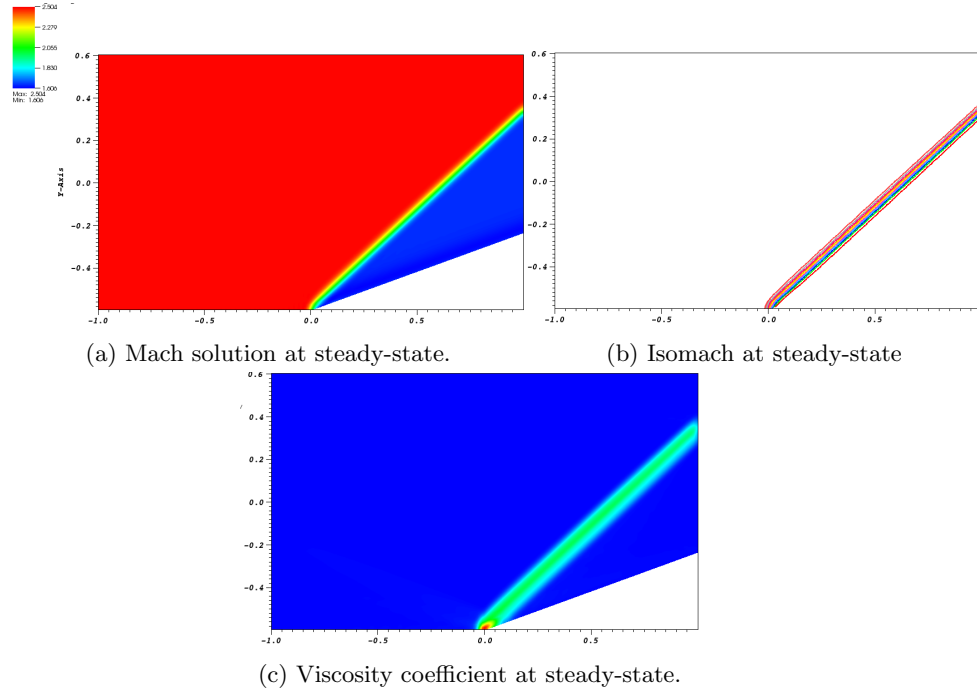


Figure 7: Steady-state solution for a flow in a 2-D compression corner.

423 **6. Conclusions**

424 **Acknowledgments**

425 **References**

- 426 [1] R. P. J-L. Guermond, Entropy viscosity method for nonlinear conservation
427 laws, *Journal of Comput. Phys* 230 (2011) 4248–4267.
- 428 [2] R. P. J-L. Guermond, Entropy viscosity method for high-order approxima-
429 tions of conservation laws, *Lecture Notes in Computational Science and*
430 *Engineering* 76 (2011) 411–418.
- 431 [3] R. P. J-L. Guermond, Entropy-based nonlinear viscosity for fourrier approx-
432 imations of conservation laws, in: *C.R. Math. Acad. Sci.*, Vol. 326, Paris,
433 2008, pp. 801–806.
- 434 [4] J. M. V. Zingan, J-L. Guermond, B. Popov, Implementation of the entropy
435 viscosity method with the discontinuous galerkin method, *Berlin: Springer*
436 253 (2013) 479–490.
- 437 [5] J.-L. Guermond, B. Popov, Viscous regularization of the euler equations and
438 entropy principles, under review.
- 439 [6] P. B., S. C-W., On positivity preserving finite volume schemes for euler
440 equations, *Numer. Math.* 73 (1996) 119–130.
- 441 [7] E. Toro, *Riemann Solvers and numerical methods for fluid dynamics*, 2nd
442 Edition, Springer, 1999.
- 443 [8] O. L. R. Berry, R. Saurel, The discrete equation method (dem) for fully
444 compressible, two-phase flows in ducts of spatially varying cross-section,
445 *Nuclear Engineering and Design* 240 (2010) 3797–3818.